PCCP

ROYAL SOCIETY OF CHEMISTRY

PAPER

View Article Online
View Journal | View Issue

Cite this: *Phys. Chem. Chem. Phys.*, 2026, **28**, 8186

Infrared free electron laser induced photodesorption of CO and N_2 from solid amorphous water at cryogenic temperatures

Kerry H. Jones, [a] Jack E. Fulker, *[b] Domantas Laurinavicius,[c] Ali Ozel,[c] Johanna. G. M. Schrauwen, [d] Britta Redlich,[d] Jennifer A. Noble, [b] Sergio Ioppolo,[e] Martin R. S. McCoustra [c] and Wendy A. Brown *[a]

Photon induced processing of molecular ices is known to be important in a number of astrophysical environments. However, to date, astrophysical models tend to only incorporate ultra-violet induced photoprocesses. This is despite the fact that the flux of infrared (IR) photons is comparable to, and sometimes exceeds that of, ultra-violet photons in a number of environments. In order to determine whether IR photoprocesses are important under astrophysical conditions, we have undertaken experiments to investigate the IR-induced desorption of CO and N_2 from CO:H_2O and N_2:H_2O mixed ices grown at 9 K. These studies were performed at FELIX, the free electron laser facility at Radboud University, Nijmegen, The Netherlands. Irradiation of the ices was performed in the mid-IR range from 2.9–12 μm and shows that photon induced desorption (PID) of CO and N_2 only occurs when the ices are irradiated at wavelengths that excite the vibrational modes of the H_2O ice. No PID is observed when the internal stretching modes of the dopant molecules are excited. The observed PID traces, recorded during the irradiation with a mass spectrometer, can be fitted with a bi-exponential decay function that shows the presence of a fast and a slow photodesorption process. These can be assigned to direct and indirect substrate-mediated resonant photodesorption processes. Power dependence studies show saturation and suggest that a complex process is leading to the observed PID. The data reported here clearly show that IR-driven photodesorption should be considered in astrophysical models.

Received 21st November 2025,
Accepted 5th March 2026

DOI: 10.1039/d5cp04525h

rsc.li/pccp

Introduction

The James Webb Space Telescope (JWST) has provided a platform that has enabled the extension of the inventory of materials contributing to icy environments in space.[1,2] The performance improvement from JWST over earlier infrared observations is such that even the weak dangling O–H features of solid water (H_2O) previously reported only in the laboratory,[3–11] are now observable.[12] However, H_2O and carbon monoxide (CO) remain the dominant molecular solids in our observed universe and are observed in many lines of sight in which ices form.[1,2,13–16] In parallel with these advancements in observational astrochemistry, laboratory experiments continue to play an important role in investigating the underlying physics that drives the changes in chemical complexity, and ultimately help us to interpret the observations.[4,17]

H_2O is observed in the mid-infrared (IR) through its fundamental vibrations at ~12 μm (the librational mode, ν_{lib}), ~6 μm (the H–O–H bending mode, ν_{bend}) and ~3 μm (the O–H stretching mode, $\nu_{stretch}$). Overtones and combination bands are also observed starting at 4.5 μm ($\nu_{lib} + \nu_{bend}$)[18] and extending through the near-IR into the visible. These contribute, with Rayleigh scattering,[19] to the pale blue colour of bulk ice and liquid water in terrestrial environments. Solid CO is also observed in the mid-IR, with its fundamental vibration observed at 4.67 μm (ν_{CO})[20] showing environmental sensitivity sufficient to identify the local environment in which the CO is observed. In contrast to CO, nitrogen (N_2) is much less abundant by a factor of around 20 and cannot be directly observed in the gas phase due to its lack of either a static or dynamic dipole moment.[21] In the solid state, however, a weak transition at 4.3 μm is observed in laboratory spectra of N_2 dispersed in

[a] *Department of Chemistry, University of Sussex, Falmer, Brighton, BN1 9QJ, UK. E-mail: w.a.brown@sussex.ac.uk*
[b] *Physique des Interactions Ioniques et Moléculaires (PIIM): CNRS, Aix-Marseille Université, Marseille, France. E-mail: jack.fulker@univ-amu.fr*
[c] *School of Engineering and Physical Sciences, Heriot-Watt University, Edinburgh, EH14 4AS, Scotland, UK*
[d] *HFML-FELIX laboratory, Radboud University, Nijmegen, 6525 ED, The Netherlands*
[e] *Department of Physics and Astronomy, University of Aarhus, Ny Munkegade 120, 8000 Aarhus C, Denmark*

water ice and other matrices due to symmetry breaking.[22–25] This weak feature has not yet been reported observationally.

Interaction of icy grains with UV photons and cosmic rays has been extensively studied and is known to promote physical processes such as desorption,[26–29] amorphisation[30–32] and crystallisation.[30,33] Such radiation also drives chemical reactions within the ices, promoting the evolution of chemical complexity in a wide range of space environments both in the solid state and in the gas phase.[34–36] This evolution in chemical complexity in the solid state contributes to the growing chemical inventory that is present in many different astrophysical environments.

To date, there are very few investigations of the effects of IR radiation on the physics and chemistry of astrophysically relevant ices. Moreover, this source of radiation, other than through its role in radiative transport,[37–40] is currently neglected in models of star and planet-forming regions. This is the case even in the situation where IR fluxes from the interstellar radiation field (ISRF) are substantially greater than the attenuated ISRF UV flux[41] and that arising from ion-electron recombination promoted by cosmic ray ionisation of H and H_2.[42,43] This is a clear short-coming of our present understanding of such processes. This is particularly the case given that the binding energy of CO to solid CO is around 6 kJ mol^{-1} (500 cm^{-1}) and that of CO to H_2O ice is 10–12 kJ mol^{-1} (830–1000 cm^{-1}).[44] These binding energies lie clearly in the energy range of IR photons and hence the lack of models incorporating IR radiation to promote non-thermal desorption is notable.

The selective IR irradiation of solid H_2O has demonstrated that desorption and restructuring of the solid H_2O can take place,[45,46] with the exact effects depending on which vibrational modes of the water are excited. A more recent study has also demonstrated IR photon induced restructuring of, and desorption from, solid CO_2 ice under astrophysically relevant conditions.[47,48] Infrared free-electron laser studies of CO irradiation in the presence of methanol ice are also reported that show photodesorption of CO.[49]

We have previously published preliminary measurements of IR photon induced desorption (PID) of CO from H_2O ice surfaces utilising the FELIX facility in The Netherlands.[50,51] Our initial work[51] describes wavelength dependent single photon IR photodesorption following excitation of the vibrational modes of H_2O. The data appear to follow bi-exponential kinetics, which we explained in terms of fast and slow desorption mechanisms. Following a significant upgrade of the free electron laser and beam line end-station at FELIX laboratory, that has improved the data quality obtained in our experiments, here we report studies of IR photodesorption of CO and N_2 from solid amorphous H_2O surfaces. These add significantly to our previous work. Indeed, the new measurements on N_2 photodesorption, which is not IR active but of the same mass as CO, allow us to confirm the ASW substrate-mediated nature of the desorption process and help us to obtain a deeper understanding of the energy transfer processes in the ice.

Methodology

Experiments were performed on the Laboratory Ice Surface Astrophysics (LISA) end station at FELIX, the free electron laser (FEL) facility at Radboud University, Nijmegen, The Netherlands. The LISA end station consists of an ultra-high vacuum (UHV) chamber equipped with facilities to perform reflection absorption infrared spectroscopy (RAIRS) and temperature programmed desorption (TPD) experiments both pre- and post-irradiation. The experimental set-up has been described in detail elsewhere,[52,53] but is briefly described here. The UHV chamber has a base pressure of $\sim 5 \times 10^{-10}$ mbar and is equipped with a pulse counting quadrupole mass spectrometer (HAL/3F RC 501, Hiden Analytical Ltd). Ices were grown *via* background vapour deposition onto the cryogenically cooled (9 K) Au-coated Cu substrate (30.6 cm^2) in the centre of the chamber permitting multiple irradiations and measurements for a single ice deposition. Cryogenic cooling of the substrate was achieved using a closed-cycle helium cryostat (ColdEdge – SRDK-101J 2.5K Cryocooler, SHI Cryogenics).

Two ice mixtures were studied: CO (Linde HiQ, 99.9%) and H_2O (deionised, purified *via* freeze–pump–thaw cycles) and N_2 (Messer CANgas, 99.9%) and H_2O. Gases were pre-mixed in the dosing line (from two separate chemical reservoirs) before deposition, with mass-independent gauges (Pfeiffer Vacuum, CCR361 and CCR 363 Ceramic Capacitance Gauges, range: 0.001–10 and 0.1–1000 mbar) used to ensure a H_2O : X target ratio of 8 : 1. Actual CO/N_2 content in the ice was determined *via* calibration TPD experiments of pure H_2O, CO, and N_2. Percentages of CO and N_2 were found to be between 11–17% with respect to water ice across several depositions. In our previous work,[51] explorations of mixtures in the composition range 6–42% of CO showed no significant change in behaviour, and so were not investigated here. The thicknesses of the resulting films were estimated to be 83.7 ± 1.2 nm for a simple amorphous solid water (ASW) film, and an average of 87.7 ± 1.2 nm for the CO:H_2O and 79.4 ± 1.1 nm for the N_2:H_2O ices. These approximate thicknesses were determined using the impingement rate of molecules on the surface over the course of the controlled background gas exposure[54] and assuming the ASW density to be 0.716 ± 0.01 g cm^{-3}.[55] This is the best estimate of the thicknesses of each ice configuration, assuming that CO and N_2 fully adsorb within the pore surfaces of the ASW matrix.

The ice growth during deposition was monitored using RAIRS with a Fourier Transform Infrared (FTIR) Spectrometer (Bruker Vertex 80v) coupled to a liquid-nitrogen-cooled mercury–cadmium–telluride detector. A total of 8 co-added scans were taken every 20 seconds during deposition. RAIR spectra were also recorded prior to and after irradiation, with the resulting spectra averaged through the co-addition of 256 scans. The infrared light from the FTIR spectrometer was directed at a grazing angle of 10° to the substrate surface, with all RAIR spectra recorded in the 5000–500 cm^{-1} range with an aperture of 1 mm and a resolution of 0.5 cm^{-1}. All RAIR spectra were baseline corrected prior to analysis.

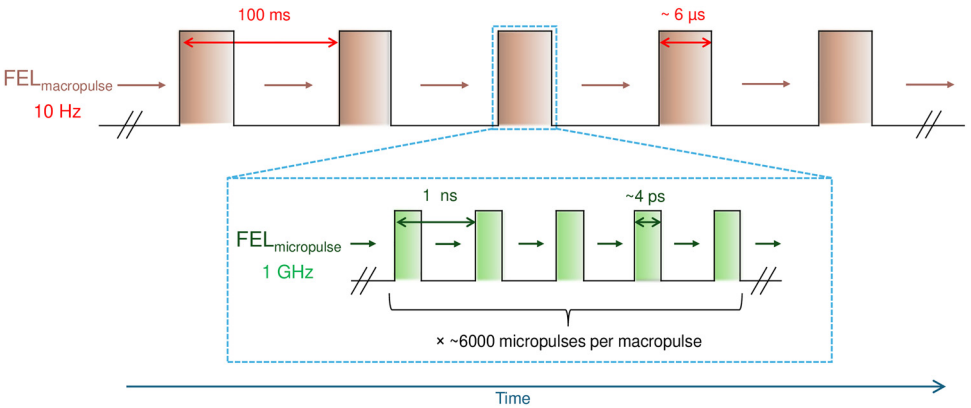

Fig. 1 Schematic of the pulse structure of the FEL-2 laser source at the FELIX facility. Shaded areas in orange and green show when the FEL-2 light is 'on' in each pulse. The blue dashed box details the micropulse structure which is present in a single macropulse. Not to scale.

Using the FEL-2 light source at the FELIX facility, ices were irradiated in the mid-infrared range (2.9–12 μm). The irradiation wavelengths were chosen to correspond to on- or off-resonance of the vibrational modes of H_2O, CO and N_2. Irradiation took place at base temperature, for a total of 1 minute. The FEL-2 beam consists of ~6 μs long macropulses at a frequency of 10 Hz (estimated from the FELIX facilty diagnostics), each containing a train of 2–6 ps long micropulses occurring at a frequency of 1 GHz, as shown in Fig. 1, and impinges on the Au-coated Cu substrate at an angle of 45° with respect to the surface.

Owing to the pulse structure of the FEL-2 beam, as shown in Fig. 1, it is necessary to account for the fraction of the total irradiation time during which the beam delivers photons. This fraction is referred to as the duty cycle, *D*. The duty cycle is calculated by taking the micropulse duration (~4 ps) multiplied by the number of micropulses in one macropulse (~6000) multiplied by the macropulse repetition rate (10 Hz). This gives a duty cycle of *ca.* 2.4×10^{-7}. This value was applied in our analysis to quantify the photodesorption behaviour. PID measurements were performed using the mass spectrometer to follow $m/z = 28$ desorption that occured during infrared irradiation of the ices corresponding to PID of CO and N_2.

The FEL-2 beam incident on the sample is monochromatic with spectral full width at half maximum (FWHM) estimated at ~0.8% $\delta\lambda/\lambda$ for the entire wavelength range. Since the substrate was significantly larger than both the RAIRS and FEL-2 laser spots, a total of 11 clean areas of the ice could be irradiated without requiring substrate cleaning or re-dosing of the ice mixture between irradiations. The energy of each macropulse of the FEL-2 beam varied with irradiation wavelength and attenuation, ranging from 2–142 mJ. Power-dependent studies were undertaken by applying increasing amounts of attenuation, ranging from 3–10 dB, to the laser source to vary the average energy of the beam. The area irradiated by the FEL-2 beam on the substrate changes depending on the irradiation wavelength, ranging from 0.0059 cm^2 at 3 μm to 0.049 cm^2 at 12 μm. Because the FTIR beam was larger than the FEL-2 beam, some significant portions of the ice probed by FTIR were not exposed to irradiation.

Fig. 2 shows RAIR spectra of the unirradiated ices composed of (a) 100% H_2O, (b) 14% CO:H_2O, and (c) 17% N_2:H_2O. The well-characterised bulk vibrational modes of ASW[18] remain unchanged in the presence of CO or N_2, as expected due to their low concentrations. The assignment of the water vibrational modes allowed the selection of the wavelengths for irradiation, as shown in Table 1. These wavelengths are associated with the water stretching (~2.9–3.1 μm), bending (~6.0 μm) and librational modes (~12.0 μm), as shown in Fig. 2. Further discussion of the RAIR spectra of the unirradiated CO and N_2 water ice mixtures is presented in the SI, specifically on the influence of the CO and N_2 on the dangling OH bands (Fig. S1).

The irradiation wavelengths chosen, and the vibrational modes they correspond to, are given in Table 1. These wavelengths were determined by recording RAIR spectra of the mixed ices (Fig. 2) and selecting the observed vibrational modes. Although an interesting potential irradiation target, the dOH modes were not chosen due to the low power of FEL-2 at this wavelength. The spectral FWHM of the FELIX beam was on the order of 0.8% $\delta\lambda/\lambda$ for all wavelengths.

As these experiments involved irradiation of both the deposited ice and the underlying substrate, the possibility of direct laser-induced thermal desorption (LITD) from the metal surface must be considered. We have therefore undertaken detailed simulations of this process, and the subsequent thermal diffusion and refrigerated cooling of our substrates, using finite element methods. Details of the simulations can be found in the SI, but briefly, two models for the heating were considered:

- The first is a model of the Au-coated Cu substrate in which the laser interaction with the metal surface is characterised using the two-temperature model.[63–65] This reflects the observation that the electromagnetic field of the IR radiation couples directly with the free electrons in the metal band structure on a timescale equivalent to the laser pulse and leads to initial heating of the electrons. However, given that the surface of the Au film is not clean in a true surface science sense, desorption *via* hot electron attachment is not likely to occur.

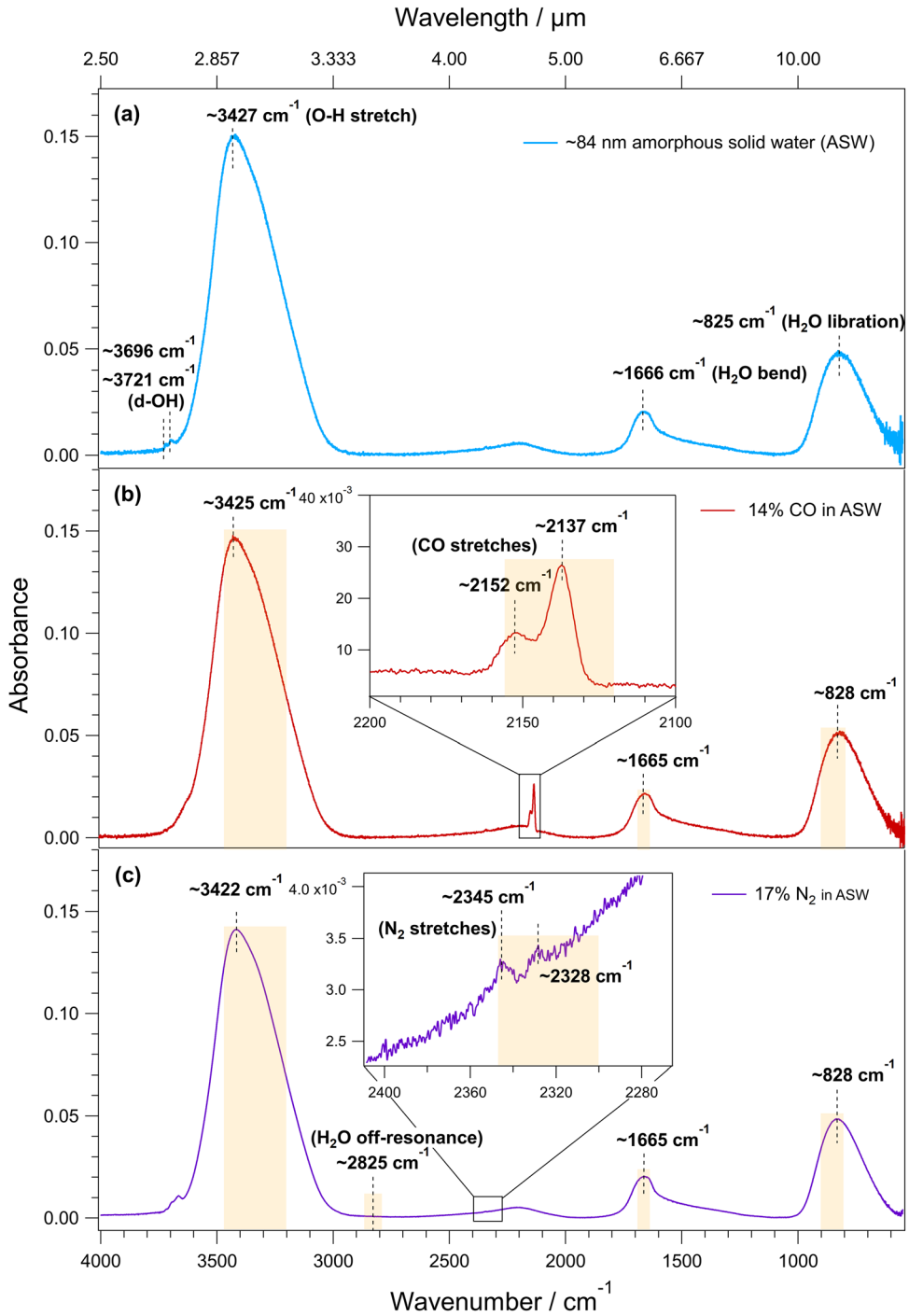

Fig. 2 RAIR spectra of (a) (83.7 ± 1.2) nm of ASW dosed on a Au-coated Cu surface at 9 K; (b) (87.7 ± 1.2) nm of a 14% CO:H_2O mixture dosed on a Au-coated Cu surface at 9 K; and (c) (79.4 ± 1.1) nm of a 17% N_2:H_2O mixture dosed on a Au-coated Cu surface at 9 K. The insets in (b) and (c) present the CO and N_2 stretching vibrations respectively. Highlighted areas show the FEL-2 wavelengths (including upper bounds) at which the CO:H_2O and N_2:H_2O ices were later irradiated, corresponding to H_2O, N_2 and CO vibrational modes as well as off-resonance wavelengths.

However, these hot electrons scatter from the metallic lattice and heat the lattice on a slower timescale. Fig. S4 illustrates the results of these calculations and shows that the lattice temperature of the Cu reaches 12.3 K, while the Au surface reaches only 10.2 K.

• The second model adds a water ice substrate on top of the Au that is thermally coupled to it. In this case, a simple model based on IR absorption within the H_2O film was added to the previous model to estimate the additional energy deposited and consequent temperature excursion due to the ps laser pulse. The experimentally measured temperature transient is shown in Fig. S5a. Fig. S6 then illustrates the results of these simulations, with the ice top layer receiving negligible heating from the laser pulses.

Table 1 Wavenumbers and corresponding band assignments for the data shown in Fig. 2. The table also shows the corresponding wavelengths and energy range at which the CO:H_2O and N_2:H_2O ices were irradiated with the FEL-2 beam

Band wavenumber/cm^{-1}	Irradiation wavelength, λ_{FEL}/μm	Irradiation energy range, E_{irr}/mJ		Band assignment
		CO:H_2O	N_2:H_2O	
3427–3422	2.92 ± 0.05, 3.00 ± 0.04, 3.10 ± 0.04	32–46	14–26	OH stretch (H_2O)[18]
2825	3.54 ± 0.05	—	63	H_2O off-resonance
2345, 2328	4.32 ± 0.04	—	62	N_2 stretch[25,56]
2152, 2137	4.68 ± 0.04	38	—	CO stretch[57–62]
1666, 1665	5.98 ± 0.04	54	59–70	H_2O bending[18]
828, 825	12.00 ± 0.07	105–127	98–142	H_2O libration[18]

By simulating the temperature profiles of each material layer in the extreme case of the total incident photon fluence acting to heat the metal substrate, we can place an upper limit on the thermal transfer into the ice. The results of these simulations indicate that while there is a degree of laser heating in the system to consider, the effects are most prominent in the bulk of the Cu, with significanly less effect at the Au surface, and even less in the ice top-layer. This therefore suggests that laser-induced thermal desorption can be assumed to be negligible in these experiments.

Results and discussion

RAIR difference spectra of irradiated CO and N_2 water ice mixtures

Investigations into the photon induced structural changes within the ices were undertaken by comparing the RAIR spectra of pre- and post-irradiated ices at each wavelength. These are reported in Fig. 3 and 4 as difference spectra, highlighting changes in the spectral profile of the O–H stretching and HOH bending modes of H_2O post-IR irradiation. We also note that we observe features at 1880 cm^{-1} which at present we are unable to identify, but given that this region is sparsely populated by common IR bands, these are most likely artefacts/mis-cancellations.

A comparison of the absorbance difference spectra for the CO:H_2O ice (Fig. 3) and the N_2:H_2O ice (Fig. 4) shows that the O–H stretching and HOH bending modes of H_2O show slightly greater absorption difference in the CO-mixed ice post-IR irradiation. This difference simply reflects variations in the maximum FEL power available during the respective experimental shifts, with higher laser power being accessible during irradiation of the CO-mixed ice than during the N_2-mixed ice experiments. It is most pronounced at 3 μm, as the maximum FEL energy during the CO-mixed ice irradiation (52 mJ) was more than double that available for the N_2-mixed ice (24 mJ).

The spectral changes observed are consistent with previously reported work in the literature and reflect the structural changes of ASW that occur as a result of irradiation.[46] Structural changes in the solid water film may result in the ejection of CO and N_2 adsorbate species. However, such processes promoted by the slow trickle down of energy into the librational heat bath are likely to contribute only to the overall slow desorption process which is discussed later.

Fig. 3b also shows a clear difference in the CO stretching mode at around 2140 cm^{-1} for the 3 and 12 μm irradiations. While this could initially be interpreted as depletion of the CO

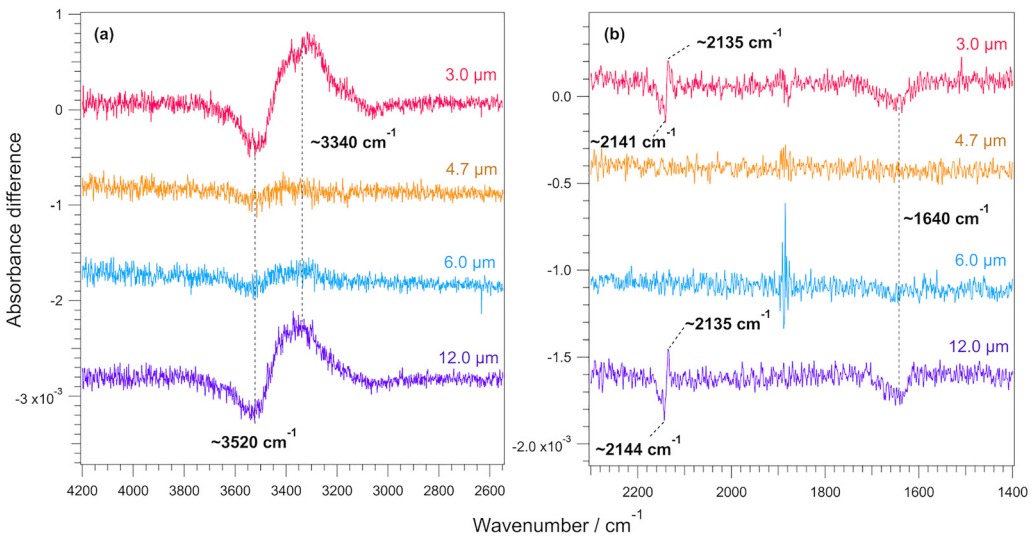

Fig. 3 RAIR difference spectra following 1-minute irradiation of a 11% CO:H_2O mixed ice. (a) shows the O–H stretching region and (b) shows the C–O stretching and O–H bending region.

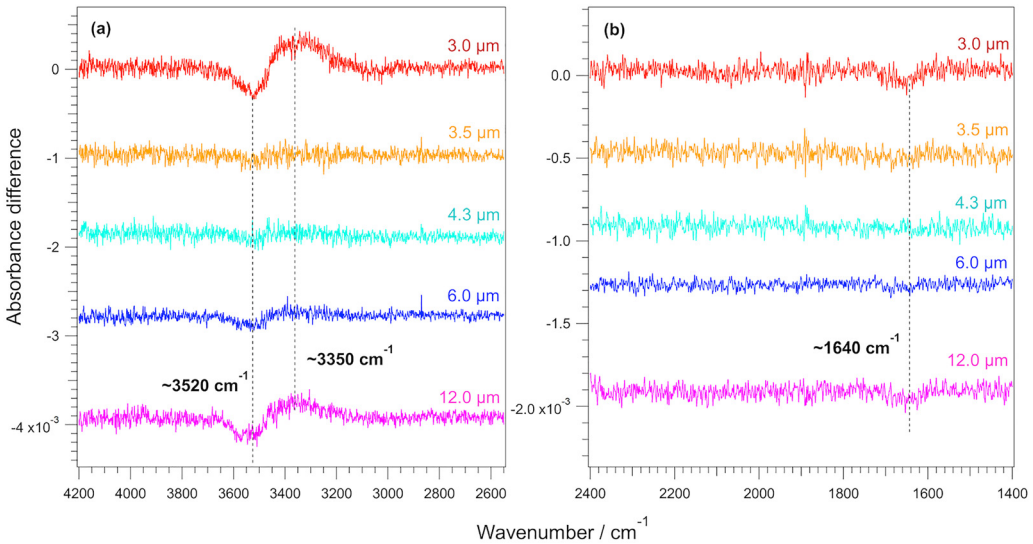

Fig. 4 RAIR difference spectra following the 1-minute irradiation of a 15% N_2:H_2O mixed ice. (a) shows the O–H stretching region and (b) shows the N_2 stretching and O–H bending region.

stretching band due to PID of CO from the water surface, given the relatively small FEL-2 spot size compared to the RAIRS spot size, it is more likely that this depletion in IR signal is an effect from the ASW restructuring, with the CO migrating to a different binding site, rather than from PID. Consequently, we cannot confidently use RAIRS as a tool for following the PID of the CO from the surface. This effect is not observed in Fig. 4b for the N_2 stretching mode in the N_2:H_2O experiments due to the low intensity of these bands.

IR photon-induced desorption of CO and N_2 from ASW

Fig. 5 shows PID traces for the CO:H_2O and N_2:H_2O ices following the desorption of m/z = 28 during irradiation of mixed ices at 3 and 12 μm. The insets show the first 1000 ms of each experiment, corresponding to the first 10/11 macropulses. As previously reported,[51] PID is observed only with excitation of the ASW substrate on the O–H stretch at 3 μm and on the librational mode at 12 μm. IR excitation of the HOH bend, and of the C–O and N–N stretching mode (detailed in Table 1) does not induce desorption, nor is desorption detected when monitoring any other masses, (*e.g.*, m/z = 18 corresponding to water desorption). Our experiments therefore show the presence of a substrate-mediated desorption process, where solid H_2O is the substrate.

The first thing of note in Fig. 5, and reflected throughout our data, is that the initial transient intensity of the CO data is smaller than that for the N_2. There are competing factors to consider here, including the N_2:ASW percentage composition (15%) being higher than that of CO:ASW (11%), which may lead to a higher N_2 desorption. However, the higher FEL energies employed in the CO experiments (36 ± 5 and 127 ± 10 mJ) compared to the N_2 experiments (25 ± 5 and 109 ± 5 mJ) might be expected to lead to higher CO desorption. While considering these as sources of variation, we conclude that the observed behaviour is more likely to reflect the relative strengths of the binding of CO and N_2 to the ASW surface,[44] with the weaker binding energy of N_2 displaying more facile IR photon-induced desorption. As we explore more systems in the future, this link between binding energy and photon-induced desorption will become clearer.

Fig. 5 also shows what appears to be typical exponential decay behaviour. However, a semi-logarithmic analysis (presented in the SI, Fig. S7) indicates that the decay does not follow a single exponential. Rather, the traces follow a bi-exponential decay that can be fitted with eqn (1). Fitting the data to this bi-exponential decay function allows the retrieval of the time constants, τ_i, for each desorption process:

$$I(t) = I_{0,1}e^{-t/\tau_1} + I_{0,2}e^{-t/\tau_2} + I_\infty \quad (1)$$

where $I_{0,i}$ is the amplitude term of each desorption component and I_∞ represents a non-zero baseline. The veracity of the bi-exponential fit to the data is shown by the comparison of single- and bi-exponential fits seen in Fig. S8. Such bi-exponential fits have been described in the literature previously by our research group as well as by others studying PID on the LISA setup.[50,51] It is possible that the data could be fitted by a higher order multi-exponential function. However, in taking such an approach we run the risk of overfitting the data. Fig. 6b shows an example of a bi-exponential fit to the CO PID data. Data are fitted by taking the peak of each individual PID feature as shown by the circles in Fig. 6a. Note that these individual peaks arise due to the pulsed nature of the FEL-2 beam as discussed previously (Fig. 1). The decay on the trailing edge of each of these individual peaks occurs due to the pumping of gas in the vacuum chamber and does not inform us of the decay kinetics of the PID process.

Table 2 details the results of the fitting of the PID data, focussing on the decay time constants, τ_i, and corresponding first order rate constants ($k_i = 1/\tau_i$). We can clearly identify the presence of a slow and fast decay channel in the time-resolved

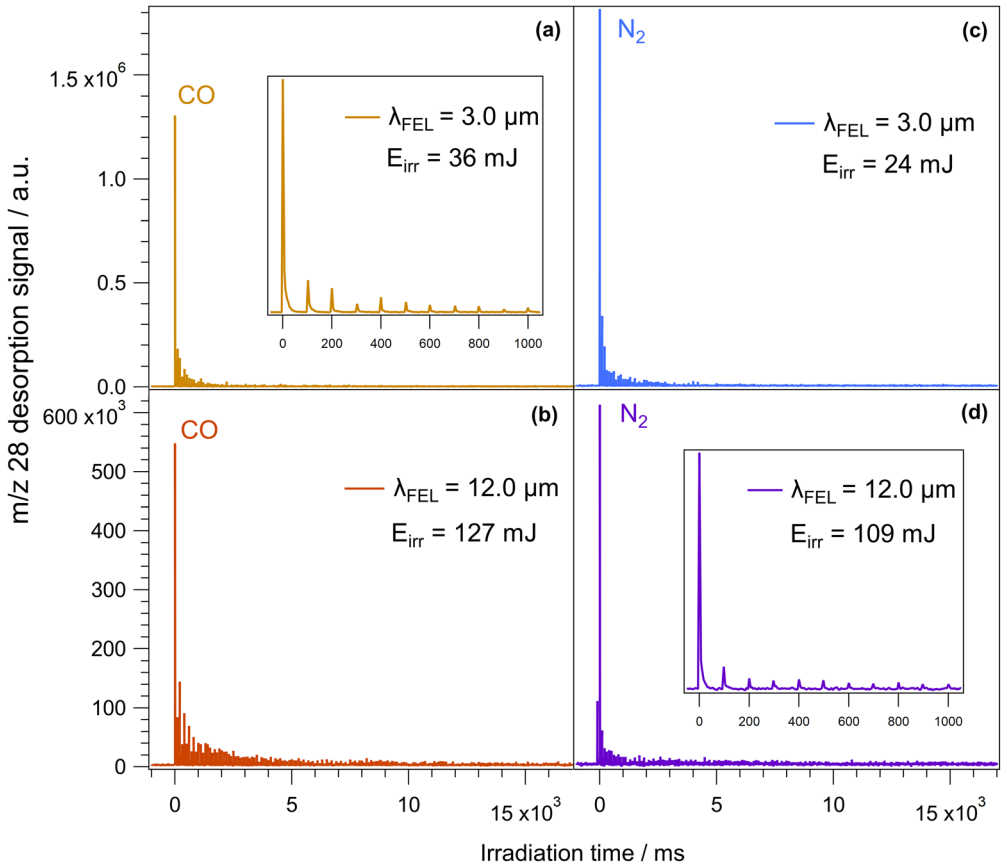

Fig. 5 m/z = 28 desorption profiles over the first 17 seconds of each 1-minute irradiation for an 11% CO:H_2O mixed ice at 9 K at (a) 3 μm (energy of 36 ± 5 mJ) and (b) 12 μm (energy of 127 ± 10 mJ). (c) and (d) show PID resulting from the irradiation of a 15% N_2:H_2O mixed ice at (c) 3 μm (energy of 24 ± 5 mJ) and (d) 12 μm (energy of 109 ± 5 mJ). The insets in (a) and (d) show the first 1000 ms of irradiation, showing the individual PID peaks in more detail.

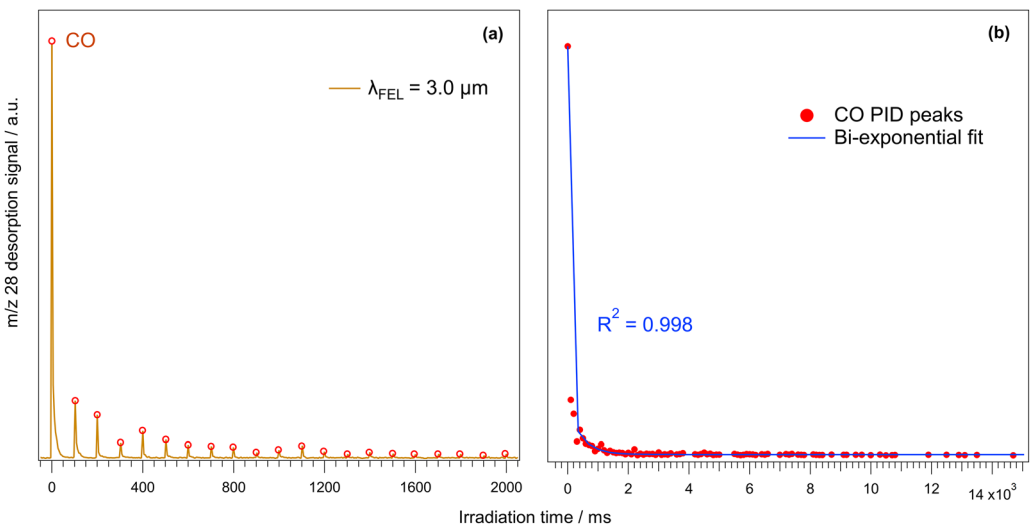

Fig. 6 The application of a bi-exponential analysis to the PID data recorded in this work. (a) shows the first 2000 ms of a 1-minute irradiation of an 11% CO:H_2O mixed ice at a wavelength of 3 μm with an energy of 36 ± 5 mJ. The PID peak transient values (circled in red) are taken for each 100 ms macropulse across the 1-minute irradiation time. These are then plotted as (b), where a bi-exponential fit (blue) is applied to the data. (b) shows only the first 15 seconds of the irradiation time in order to show the bi-exponential fit in detail.

PID data. Table S2 reports the I_i for various laser pulse energies and shows the additional observation that the ratio I_1/I_2 is around 9 for excitation of the CO:H_2O and N_2:H_2O ices at 3 μm. At 12 μm this ratio is more variable, ranging from ~3–12.

Table 2 The average time constants τ_i (scaled using the duty cycle D), and the rate constants k for fast and slow photon-induced desorption processes. These were calculated using a bi-exponential fit to the photodesorption traces recorded during irradiation of the CO:H_2O and N_2:H_2O mixed ices at 3 and 12 μm. The full list of individual experiments and their resulting values for these parameters can be found in the SI (Table S2)

Ice configuration, X:H_2O	Average irradiation wavelength, λ_{FEL}	Average time constants, ($\tau \times D$)		Average rate constants, k	
X	λ_{FEL}/μm	$\tau_1/10^{-8}$ s	$\tau_2/10^{-8}$ s	$k_1/10^7$ s^{-1}	$k_2/10^7$ s^{-1}
CO	3	1.31 ± 0.01	21.47 ± 0.60	7.64 ± 0.08	0.47 ± 0.01
	12	1.53 ± 0.15	28.81 ± 6.07	6.52 ± 0.66	0.35 ± 0.07
N_2	3	1.20 ± 0.01	26.55 ± 3.44	8.34 ± 0.07	0.38 ± 0.05
	12	1.60 ± 0.11	35.79 ± 0.05	6.26 ± 0.44	0.28 ± 0.0004

Even with the variation at 12 μm this ratio indicates that at both excitation wavelengths the fast channel predominates over the slow channel in leading to most of the observed PID intensity.

In our previous work,[51] we speculated on the mechanisms at play in the PID process for CO desorption from a mixed CO:H_2O ice. The measurements reported here support the idea that the dominant fast process is associated with resonant excitation of the vibrational modes of water in the surface of the ice to which CO or N_2 is weakly bound. Considering that the binding energies of CO (or N_2) on ASW range from 8.1 kJ mol^{-1} (7.5 kJ mol^{-1}) at saturation to around 14.1 kJ mol^{-1} (13.3 kJ mol^{-1}),[66] a 3 μm photon clearly possesses sufficient energy (39.9 kJ mol^{-1}) to overcome the dissociation barrier holding the CO (or N_2) to the ice. However, when we consider the 12 μm photon (10 kJ mol^{-1}) then we see that this photon is only capable of desorbing the weakly bound CO (or N_2). Excitation at both 3 and 12 μm should therefore cause desorption. However, the latter is likely to desorb only a fraction of the CO (or N_2) and therefore results in a generally weaker signal.

Excitation at 3 μm of the O–H stretching mode most likely promotes a kick-off mechanism, where the extension of the O–H bond in the $v = 1$ vibrational state effectively shortens the OH···CO interaction distance. This places the CO in a more repulsive environment and subsequently kicks it off the surface. If there are any second layer CO or N_2 species present, then the Newton's Cradle mechanism observed by Arnolds and co-workers[70] will likely come into play. We can thus describe both IR PID mechanisms as being substrate-mediated or indirect resonant photodesorption, in contrast to the adsorbate-mediated or direct resonant photodesorption *via* CO (N_2) excitation which we do not observe. However, as our measurement convolves all the processes occurring following photon absorption, we must consider what happens to the energy deposited in the ice following excitation. Energy flow in water (both liquid and amorphous solid) has been extensively studied.[67] The work of Yu *et al.* summarises the flow of vibrational energy once deposited into a target O–H stretching vibration,[68] with Förster coupling (non-radiative dipole coupled energy transfer) operating on a sub-100 fs timescale to surrounding O–H stretches.[69] Therefore, if the O–H absorbing the primary photon is not directly participating in the binding of a CO or N_2, Förster coupling will diffuse the energy over the surface until such a site is found and CO (or N_2) can be desorbed. In parallel, but on a longer timescale (+200 fs), vibrational relaxation will occur of the initially excited O–H stretch into the libration. We know that exciting the libration brings sufficient energy to cause desorption of the weakly bound CO (or N_2). Hence as energy trickles down from above, a second CO (or N_2) consecutive desorption channel will present itself, which accounts for the bi-exponential behaviour of the 3 μm decay data. Pumping the 12 μm band directly cuts out the intermediate relaxation processes, and the desorption process is then reduced to reflecting the fast mechanical processes associated with the CO (or N_2) desorption. These are likely to be on a similar timescale to those at 3 μm and hence the similarity in the fast components of the decays following excitation at 3 and 12 μm.

IR photon-induced desorption power dependence of CO and N_2

In photodesorption processes, the peak desorption signal at $t = 0$, I_0, scales with laser power, in terms of the photon fluence, F (photons cm^{-2}). Using eqn (2) and taking the natural logarithm of the peak desorption signal at $t = 0$, I_0, *versus* the natural logarithm of the photon fluence, the gradient gives the photon order, n:

$$I_0 \propto F^n \tag{2}$$

Considering the pulse structure of the FEL-2 beam as shown in Fig. 1, the energy recorded with the power meter is both the average energy of a single macropulse, and the summation of every micropulse energy within one macropulse. Photon fluence, F, *is* therefore calculated using eqn (3):

$$F = \frac{E_{FEL}}{E_{photon}} \times \frac{1}{A_{beam}} \tag{3}$$

where E_{FEL} is the average energy of each macropulse, A_{beam} is the FEL-2 spot size on the surface, and E_{photon} is the energy of each photon within a micropulse. Power dependence calculations were performed exclusively for desorption at 3 μm with a spot size of 0.0059 cm^2, as the available experimental data at 12 μm were insufficient for reliable analysis.

Fig. 7 shows a logarithmic plot of the initial macropulse intensity, I_0, for each irradiation experiment as a function of the calculated fluence, obtained at a series of FEL-2 laser powers at 3 μm with varying attenuation levels, following either CO or N_2 desorption. The photon orders were extracted from the gradients in regions where a clear monotonic increase was observed, giving orders of approximately 2, which would generally imply a

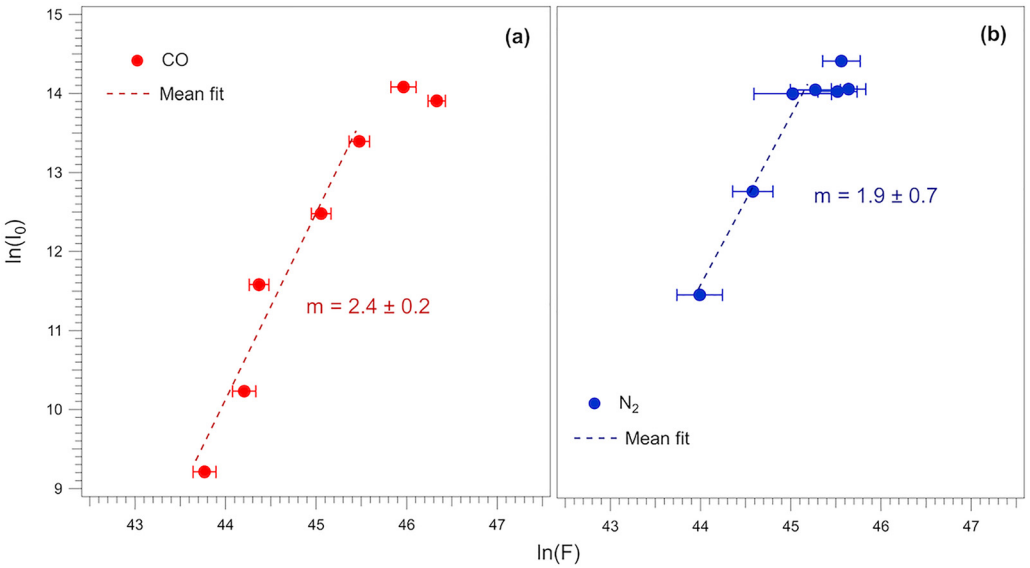

Fig. 7 Laser fluence, F (photons cm^{-2}), dependence of PID I_0 for 3 μm irradiation of (a) CO on ASW and (b) N_2 on ASW.

multiphoton process. However, given the calculated fluence, it is highly unlikely that each water molecule is absorbing two photons per desorption event, and so the determined photon order of 2 relates more to a complex mechanism of energy transfer within the water matrix, rather than a traditional multiphoton process. Further to this, Fig. 7 shows that beyond a certain fluence threshold, I_0 no longer increases and instead exhibits a plateau. This occurs at $\sim 9.2 \times 10^{19}$ photon cm^{-2} ($\sim$36 mJ) for CO, and $\sim 5.9 \times 10^{19}$ photon cm^{-2} ($\sim$23 mJ) for N_2. This suggests that beyond this fluence threshold, the PID behaviour is no longer influenced by the laser fluence. In this regime, the PID can be considered independent of fluence and is said to be saturated. Such saturation generally occurs when the excitation and relaxation rates in a multi-level optical system are competitive.[71]

Saturation behaviour is well known in IR laser pumped systems[72,73] having been observed soon after the development of optical and IR lasers in the 1960s. In the IR, ladder climbing mechanisms are commonly employed to describe phenomena such as IR multiphoton dissociation in the gas phase.[74,75] In the gas phase, ladder climbing mechanisms are supported by the Stark broadening of (ro)vibrational energy levels permitting consecutive absorption of photons of fixed frequency within the manifold of (ro)vibrational states, and by the relatively slow relaxation of excited (ro)vibrational states.[76] Hence, the facility for consecutive absorption of IR photons within a vibrational manifold in the solid state is feasible. However, vibrational relaxation mechanisms are more efficient in the solid state. Bonn and co-workers have reported direct measurements of the O–H stretch relaxation times in crystalline solid water on the 100 fs timescale and on the 100 s of fs for liquid water.[77] ASW, as employed in the current experiments, is more likely to behave like liquid water. Estimates of the vibrational linewidth, and hence vibrational lifetime, are consistent with this observation.[78,79] Thus, in the present case, relaxation of the pumped O–H stretch competes with the ps timescale of the IR excitation and de-excitation by stimulated emission. The observation of saturation and multi-photon power dependence (Fig. 7) is therefore evidence of a ladder climbing mechanism driven by the ps laser excitation.[71] This is likely enabled by the relatively broad spectral width of the FEL and the relatively harmonic, yet solid state broadened, O–H stretch which allows for consecutive excitations without the Stark Broadening that is typical in the gas phase.

Fig. 8 shows this proposed ladder climbing mechanism involving a sequence of consecutive one-photon absorption processes taking us from $v = 0$ to $v = 2$ (given that our photon order is two) in the O–H stretching potential energy well. While this model currently only shows three levels, the model can be extended to include higher energy levels.

If we consider the $v = 0$ to $v = 1$ excitation on the O–H stretch, the rate of relaxation of the $v = 1$ state will determine the propensity to saturation. We can identify radiative and non-radiative relaxation mechanisms: (i) spontaneous emission ($k_{\text{sp.em.},10}$), (ii) stimulated emission ($k_{\text{st.em.},10}$), (iii) IVR populating the librational (12 μm) heat sink ($k_{\text{IVR,AB}}$), (iv) IVR populating the low energy lattice vibrational heat sink ($k_{\text{IVR,AC}}$), and (v) IR PID ($k_{\text{PID,A1}}$). The vibrational relaxation of excited O–H stretches has been explored independently by Sudera *et al.* using ultrafast time-resolved IR spectroscopy, pointing to a decay mechanism through two intermolecular vibrational energy redistribution (IVR) channels.[77] We link these channels to populating the 12 μm libration (frustrated rotational modes) and the much lower in energy "lattice vibrational heat sink" (frustrated translational modes) of the ice film. Kinetically these processes occur in parallel and we can write:

$$k_{\text{relaxation,A1}} = k_{\text{sp.em.},10} + k_{\text{st.em.},10} + k_{\text{IVR,AB}} + k_{\text{IVR,AC}} + k_{\text{PID,A1}} \quad (4)$$

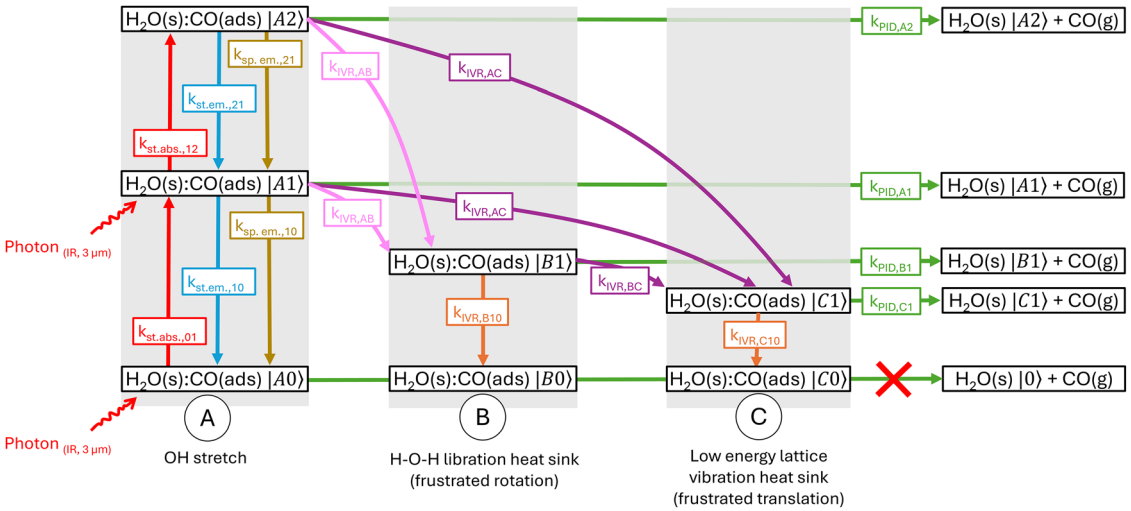

Fig. 8 Proposed ladder climbing mechanism for the 3 μm pumping of the CO:H_2O system showing the first three energy levels involved in consecutive one-photon absorptions. Transitions between levels are achieved *via* stimulated absorption ($k_{st.abs,ij}$), stimulated emission ($k_{st.em,ij}$), spontaneous emission ($k_{sp.em,ij}$), and intermolecular vibrational energy redistribution ($k_{IVR,ij}$) to the H_2O libration mode and low energy lattice vibrations. CO removal from the condensed phase is achieved *via* PID from each of the vibrationally excited states ($k_{PID,i}$).

with

$$k_{st.em.,10} = \sigma_{10} \times F \quad (5)$$

where σ_{10} is the cross-section for stimulated emission and F is the laser fluence. In addition, if we consider a contribution of $v = 1$ to $v = 2$ up-pumping, $k_{st.abs,12}$, which itself is proportional to the laser fluence, then the rate constant for the decay of the PID signal following excitation at 3 μm will exhibit a fluence dependence reflecting the sum of these two optically driven processes.

The competition between these processes has the effect of decreasing the population of the $v = 1$ state as a function of optical power due to the relation in eqn (5) (and the eqivalent for $k_{st.abs,12}$). The decay lifetime of the $v = 1$ population will therefore decrease, as shown in Fig. S9 for the CO:H_2O experiments. The observed trend in the case of CO is consistent with this proposition, and we can conclude that the observation of this laser power dependence on the rate constant supports our proposal of a ladder climbing mechanism at play.

We observe that direct excitation of the 12 μm libration mode results in PID and speculate that this might be occurring *via* three potential mechanisms. In the first, a single 12 μm photon carries sufficient energy to excite PID from the most weakly bound CO (N_2) sites on the surface. However, given the substantially higher laser pulse energies available at 12 μm and noting that the photon absorption cross-section at 12 μm is not incomparable to that at 3 μm, then we might expect rapid ladder climbing up the librational manifold in the lifetime and Stark broadened solid-state environment during the irradiation of the ASW. At the 4-photon level in this manifold, there is an energy correspondence to the one photon level in the O–H manifold that could provide a gateway to repopulating that energy level. Of course, such a process is not relevant in astrophysical environments but should be considered in explaining our experiments. Finally, excitation of the 12 μm vibration by energy redistribution from the 3 μm O–H stretch excitation will likely also promote PID. This process is consecutive to the up-pumping which directly produces a component of the PID and may account for the bi-exponential nature of the PID decays. The observation of bi-exponential decays following 12 μm excitation may point to another desorption pathway in the system. This may be linked to the localised structural change in the water ice promoting reduction in CO and N_2 binding energy.

The question that arises then is how much of the transient IR PID signal derives from each of the excited states and how our experimentally derived rate constants (k_1 and k_2 for the fast and slow PID processes) relate to desorption from each state. We are currently exploring this through kinetic modelling and a publication detailing both the 3 μm and 12 μm pumping systems is currently in preparation.

Under this proposed ladder-climbing mechanism, PID cross-sections, and therefore quantum yields, are significantly more complicated to retrieve than in simple single-photon absorption cases, as the observed PID arises from a convolution of sequential one-photon absorptions.

While an effective desorption cross-section and quantum yield can be calculated, these are currently only preliminary values and will be reported with the results of the kinetic modelling.

Astrophysical impact and conclusions

The present work clearly identifies a substrate (solid water) mediated IR PID channel for CO and N_2 adsorbed on the surface of ASW. This is entirely consistent with our previous report in a recent Faraday discussion.[51] In that earlier paper, we reported that the IR PID of CO showed single photon behaviour

and highlighted the potential astronomical importance of IR PID as a mechanism for returning ice surface bound species to the gas phase in cold, dense environments where IR photons dominate over the UV.

PID of both CO and N_2 from binary mixed ices with ASW show almost identical behaviour, indicating that this PID mechanism is most likely the same in both cases. Both species have similar binding energies, with CO being slightly higher due to exhibiting both dipole electrostatic interactions and dispersion interactions with the water surface, while N_2 exhibits weaker quadrupolar electrostatic interactions and dispersion interactions. This is confirmed by the measured binding energies reported in the literature.[44] This is in line with our experimental observations of N_2 undergoing greater initial PID (I_0) and having a higher rate constant for the 3 μm fast process (k_1).

Our current work, following a major upgrade of FEL-2 and of the LISA end-station at the FELIX facility, has revealed more complex behaviour with the observation of saturation in the power dependent PID data. Our interpretation of that data is consistent with a ladder climbing mechanism that would point to consecutive single photon events that excite the O–H stretch of the water from the $v = 0$ to $v = 1$ and then from $v = 1$ to $v = 2$. From these excited vibrational states, exit channels along the desorption coordination of the CO and N_2 become available as the photon energies of these transitions far exceeds the binding energies of the two diatomic species. With kinetic modelling of this process underway that will confirm our proposition and reveal the relative proportions of exit from $v = 1$ *versus* $v = 2$, these studies affirm the need to re-address the role of IR-driven photodesorption in astrophysical environments.

Author contributions

Kerry H. Jones – experiments, data analysis, writing – original draft, data interpretation and commented on the paper. Jack E. Fulker – data analysis, writing – original draft, data interpretation and commented on the paper. Domantas Laurinavicius – experiments and commented on the paper. Ali Ozel – simulations, data interpretation and commented on the paper. Johanna. G. M. Schrauwen – experiments and commented on the paper. Britta Redlich – initiation and management of the project and commented on the paper. Jennifer A. Noble – experiments, data interpretation and commented on the paper. Sergio Ioppolo – experiments, data interpretation and commented on the paper. Martin R. S. McCoustra – initiation and management of the project, experiments, data analysis, writing – original draft, data interpretation and commented on the paper. Wendy A. Brown – initiation and management of the project, experiments, data analysis, writing – original draft, data interpretation and commented on the paper.

Conflicts of interest

There are no conflicts of interest.

Data availability

Raw experimental data and computational output files are available and can be found at the University of Sussex data repository https://doi.org/10.25377/sussex.30667676.

Supplementary information (SI) is available. See DOI: https://doi.org/10.1039/d5cp04525h.

Acknowledgements

The authors would like to thank Dr J. Thrower (Aarhus University) for generating optical models based on the Greenler Equations for RAIRS and helpful discussions during the project. The authors would also like to thank Dr E. R. Ingman (NASA/American University) for her contributions to this work in the earlier stages of the project. All authors thank HFML-FELIX for the allocation of beamtime and specifically the FELIX operators for their assistance during beamtime shifts. The main components of the LISA experimental apparatus were purchased using funding obtained from the Royal Society through grants UF130409, RGF/EA/180306, and URF/R/191018. KHJ and DL thank the University of Sussex and a Heriot Watt University EPSRC DTP program respectively for their studentships supporting their PhD studies. They both acknowledge travel support from the UK Engineering and Physical Sciences Research Council (UK EPSRC). JEF and JAN acknowledge support from the Thematic Action ''Physique et Chimie du Milieu Interstellaire'' (PCMI) of INSU Programme National ''Astro'', with contributions from CNRS Physique & CNRS Chimie, CEA, and CNES and funding from the Agence Nationale de la Recherche (ANR, HYDRAE project ANR-21-CE30-0004-01). JGMS acknowledges this publication as part of the project ''HFML-FELIX: a Dutch Centre of Excellence for Science under Extreme Conditions'' (with project number 184.035.011) of the research programme ''Nationale Roadmap Grootschalige Wetenschappelijke Infastructuur'' which is (partly) financed by the Dutch Research Council (NWO). SI thanks the Danish National Research Foundation through the Center of Excellence ''InterCat'' (Grant agreement no.: DNRF150) and the Royal Society for financial support. MMcC wishes to acknowledge the UK Engineering and Physical Science Research Council (EPSRC) for support in the form of a research grant entitled ''Astrocatalysis: In operando Studies of Catalysis and Photocatalysis of Space-abundant Transition Metals'' (grant no. EP/W023024/1). We thank the reviewers for their comments on the manuscript, through which the strength and overall coherence of the article was improved.

References

1 M. K. McClure, W. R. M. Rocha, K. M. Pontoppidan, N. Crouzet, L. E. U. Chu, E. Dartois, T. Lamberts, J. A. Noble, Y. J. Pendleton, G. Perotti, D. Qasim, M. G. Rachid, Z. L. Smith, F. Sun, T. L. Beck, A. C. A. Boogert, W. A. Brown, P. Caselli, S. B. Charnley, H. M. Cuppen, H. Dickinson, M. N. Drozdovskaya, E. Egami, J. Erkal, H. Fraser,

R. T. Garrod, D. Harsono, S. Ioppolo, I. Jiménez-Serra, M. Jin, J. K. Jørgensen, L. E. Kristensen, D. C. Lis, M. R. S. McCoustra, B. A. McGuire, G. J. Melnick, K. I. Öberg, M. E. Palumbo, T. Shimonishi, J. A. Sturm, E. F. Van Dishoeck and H. Linnartz, *Nat. Astron.*, 2023, **7**, 431–443.

2 J. A. Sturm, M. K. McClure, T. L. Beck, D. Harsono, J. B. Bergner, E. Dartois, A. C. A. Boogert, J. E. Chiar, M. A. Cordiner, M. N. Drozdovskaya, S. Ioppolo, C. J. Law, H. Linnartz, D. C. Lis, G. J. Melnick, B. A. McGuire, J. A. Noble, K. I. Öberg, M. E. Palumbo, Y. J. Pendleton, G. Perotti, K. M. Pontoppidan, D. Qasim, W. R. M. Rocha, H. Terada, R. G. Urso and E. F. Van Dishoeck, *Astron. Astrophys.*, 2023, **679**, A138.

3 B. Rowland and J. P. Devlin, *J. Chem. Phys.*, 1991, **94**, 812–813.

4 M. McCoustra and D. A. Williams, *Mon. Not. R. Astron. Soc.*, 1996, **279**, L53–L56.

5 M. E. Palumbo, *Astron. Astrophys.*, 2006, **453**, 903–909.

6 J. A. Noble, C. Martin, H. J. Fraser, P. Roubin and S. Coussan, *J. Phys. Chem. Lett.*, 2014, **5**, 826–829.

7 S. Coussan, J. A. Noble, H. M. Cuppen, B. Redlich and S. Ioppolo, *J. Phys. Chem. A*, 2022, **126**, 2262–2269.

8 S. Coussan, P. Roubin and J. A. Noble, *Phys. Chem. Chem. Phys.*, 2015, **17**, 9429–9435.

9 J. A. Noble, C. Martin, H. J. Fraser, P. Roubin and S. Coussan, *J. Phys. Chem. C*, 2014, **118**, 20488–20495.

10 K. P. Stevenson, G. A. Kimmel, Z. Dohnálek, R. S. Smith and B. D. Kay, *Science*, 1999, **283**, 1505–1507.

11 B. Maté, M. Á. Satorre and R. Escribano, *Phys. Chem. Chem. Phys.*, 2021, **23**, 9532–9538.

12 J. A. Noble, H. J. Fraser, Z. L. Smith, E. Dartois, A. C. A. Boogert, H. M. Cuppen, H. J. Dickinson, F. Dulieu, E. Egami, J. Erkal, B. M. Giuliano, B. Husquinet, T. Lamberts, B. Maté, M. K. McClure, M. E. Palumbo, T. Shimonishi, F. Sun, J. B. Bergner, W. A. Brown, P. Caselli, E. Congiu, M. N. Drozdovskaya, V. J. Herrero, S. Ioppolo, I. Jimenez-Serra, H. Linnartz, G. J. Melnick, B. A. McGuire, K. I. Oberg, G. Perotti, D. Qasim, W. R. M. Rocha and R. G. Urso, *Nat. Astron.*, 2024, **8**, 1169–1180.

13 A. Moneti, J. Cernicharo and J. R. Pardo, *Astrophys. J.*, 2001, **549**, L203–L207.

14 K. I. Öberg, A. C. A. Boogert, K. M. Pontoppidan, S. Van Den Broek, E. F. Van Dishoeck, S. Bottinelli, G. A. Blake and N. J. Evans, *Astrophys. J.*, 2011, **740**, 109.

15 E. L. Gibb, D. C. B. Whittet, A. C. A. Boogert and A. G. G. M. Tielens, *Astrophys. J., Suppl. Ser.*, 2004, **151**, 35–73.

16 A. Boogert, P. Gerakines and D. Whittet, *Annu. Rev. Astron. Astrophys.*, 2015, **53**, 541–581.

17 W. R. M. Rocha, M. G. Rachid, B. Olsthoorn, E. F. Van Dishoeck, M. K. McClure and H. Linnartz, *Astron. Astrophys.*, 2022, **668**, A63.

18 W. Hagen, A. G. G. M. Tielens and J. M. Greenberg, *Chem. Phys.*, 1981, **56**, 367–379.

19 C. F. Bohren and D. R. Huffman, *Absorption and Scattering of Light by Small Particles*, Wiley-Interscience, New York, 1st edn, 1998.

20 G. E. Ewing and G. C. Pimentel, *J. Chem. Phys.*, 1961, **35**, 925–930.

21 M. A. Frerking, J. Keene, G. A. Blake and T. G. Phillips, *Astrophys. J.*, 1989, **344**, 311–319.

22 B. Nelander, *Chem. Phys. Lett.*, 1976, **42**, 187–189.

23 S. A. Sandford, M. P. Bernstein, L. J. Allamandola, D. Goorvitch and T. C. V. S. Teixeira, *Astrophys. J.*, 2001, **548**, 836–851.

24 E. Quirico, B. Schmitt, R. Bini and P. R. Salvi, *Planet. Space Sci.*, 1996, **44**, 973–986.

25 M. P. Bernstein and S. A. Sandford, *Spectrochim. Acta, Part A*, 1999, **55**, 2455–2466.

26 K. I. Öberg, G. W. Fuchs, Z. Awad, H. J. Fraser, S. Schlemmer, E. F. Van Dishoeck and H. Linnartz, *Astrophys. J.*, 2007, **662**, L23–L26.

27 K. I. Öberg, E. F. Van Dishoeck and H. Linnartz, *Astron. Astrophys.*, 2009, **496**, 281–293.

28 K. I. Öberg, H. Linnartz, R. Visser and E. F. Van Dishoeck, *Astrophys. J.*, 2009, **693**, 1209–1218.

29 M. Bertin, E. C. Fayolle, C. Romanzin, H. A. M. Poderoso, X. Michaut, L. Philippe, P. Jeseck, K. I. Öberg, H. Linnartz and J.-H. Fillion, *Astrophys. J.*, 2013, **779**, 120.

30 D. V. Mifsud, P. A. Hailey, P. Herczku, Z. Juhász, S. T. S. Kovács, B. Sulik, S. Ioppolo, Z. Kaňuchová, R. W. McCullough, B. Paripás and N. J. Mason, *Eur. Phys. J. D*, 2022, **76**, 87.

31 M. H. Moore and R. L. Hudson, *Astrophys. J.*, 1992, **401**, 353–360.

32 G. Strazzulla, G. A. Baratta, G. Leto and G. Foti, *Europhys. Lett.*, 1992, **18**, 517–522.

33 P. Ehrenfreund, O. Kerkhof, W. A. Schutte, A. C. A. Boogert, P. A. Gerakines, E. Dartois, L. D'Hendecourt, A. G. G. M. Tielens, E. F. van Dishoeck and D. C. B. Whittet, *Astron. Astrophys.*, 1999, **350**, 240–253.

34 Q. T. Wu, H. Anderson, A. K. Watkins, D. Arora, K. Barnes, M. Padovani, C. N. Shingledecker, C. R. Arumainayagam and J. B. R. Battat, *ACS Earth Space Chem.*, 2024, **8**, 79–88.

35 C. R. Arumainayagam, R. T. Garrod, M. C. Boyer, A. K. Hay, S. T. Bao, J. S. Campbell, J. Wang, C. M. Nowak, M. R. Arumainayagam and P. J. Hodge, *Chem. Soc. Rev.*, 2019, **48**, 2293–2314.

36 K. I. Öberg, *Chem. Rev.*, 2016, **116**, 9631–9663.

37 *Radiative processes in astrophysics*, ed. G. B. Rybicki and A. P. Lightman, Wiley VCH, Weinheim, 2004.

38 R. Kuiper, H. Klahr, C. Dullemond, W. Kley and T. Henning, *Astron. Astrophys.*, 2010, **511**, A81.

39 J. Steinacker, M. Baes and K. D. Gordon, *Annu. Rev. Astron. Astrophys.*, 2013, **51**, 63–104.

40 R. Wünsch, *Front. Astron. Space Sci.*, 2024, **11**, 1346812.

41 J. S. Mathis, P. G. Mezger and N. Panagia, *Astron. Astrophys.*, 1983, **128**, 212–229.

42 S. S. Prasad and S. P. Tarafdar, *Astrophys. J.*, 1983, **267**, 603–609.

43 C. J. Shen, J. M. Greenberg, W. A. Schutte and E. F. Van Dishoeck, *Astron. Astrophys.*, 2004, **415**, 203–215.

44 M. Minissale, Y. Aikawa, E. Bergin, M. Bertin, W. A. Brown, S. Cazaux, S. B. Charnley, A. Coutens, H. M. Cuppen,

V. Guzman, H. Linnartz, M. R. S. McCoustra, A. Rimola, J. G. M. Schrauwen, C. Toubin, P. Ugliengo, N. Watanabe, V. Wakelam and F. Dulieu, *ACS Earth Space Chem.*, 2022, **6**, 597–630.
45 C. Focsa, B. Chazallon and J. L. Destombes, *Surf. Sci.*, 2003, **528**, 189–195.
46 H. M. Cuppen, J. A. Noble, S. Coussan, B. Redlich and S. Ioppolo, *J. Phys. Chem. A*, 2022, **126**, 8859–8870.
47 S. Ioppolo, J. A. Noble, A. Traspas Muiña, H. M. Cuppen, S. Coussan and B. Redlich, *J. Mol. Spectrosc.*, 2022, **385**, 111601.
48 J. G. M. Schrauwen, T. M. Dijkhuis, S. Ioppolo, D. R. Galimberti, B. Redlich and H. M. Cuppen, *ACS Earth Space Chem.*, 2025, **9**, 1580–1592.
49 J. C. Santos, K.-J. Chuang, J. G. M. Schrauwen, A. Traspas Muiña, J. Zhang, H. M. Cuppen, H. Linnartz and S. Ioppolo, *Astron. Astrophys.*, 2023, **672**, A112.
50 L. Slumstrup, J. D. Thrower, J. G. M. Schrauwen, T. Lamberts, E. R. Ingman, D. Laurinavicius, J. DeVine, J. Terwisscha Van Scheltinga, J. C. Santos, J. A. Noble, G. Wenzel, M. R. S. McCoustra, W. A. Brown, H. Linnartz, L. Hornekær, H. M. Cuppen, B. Redlich and S. Ioppolo, *ACS Earth Space Chem.*, 2025, **9**, 1607–1621.
51 E. R. Ingman, D. Laurinavicius, J. Zhang, J. G. M. Schrauwen, B. Redlich, J. A. Noble, S. Ioppolo, M. R. S. McCoustra and W. A. Brown, *Faraday Discuss.*, 2023, **245**, 446–466.
52 S. Ioppolo, J. A. Noble, A. Traspas Muiña, H. M. Cuppen, S. Coussan and B. Redlich, *J. Mol. Spectrosc.*, 2022, **385**, 111601.
53 J. G. M. Schrauwen, H. M. Cuppen, S. Ioppolo and B. Redlich, *Astron. Astrophys.*, 2024, **691**, A209.
54 J. E. Fulker, M. McCoustra and W. A. Brown, *ACS Earth Space Chem.*, 2025, **9**, 746–756.
55 R. L. Hudson and Y. Y. Yarnall, *ACS Earth Space Chem.*, 2026, **10**, 603–613.
56 T. L. Ellington and G. S. Tschumper, *Comput. Theor. Chem.*, 2013, **1021**, 109–113.
57 E. R. Ingman, PhD Thesis, University of Sussex, 2023.
58 H. J. Fraser, M. P. Collings, J. W. Dever and M. R. S. McCoustra, *Mon. Not. R. Astron. Soc.*, 2004, **353**, 59–68.
59 M. E. Palumbo and G. Strazzulla, *Astron. Astrophys.*, 1993, **269**, 568–580.
60 B. Schmitt, J. M. Greenberg and R. J. A. Grim, *Astrophys. J.*, 1989, **340**, L33–L36.
61 M. P. Collings, J. W. Dever and M. R. S. McCoustra, *Phys. Chem. Chem. Phys.*, 2014, **16**, 3479.
62 M. P. Collings, J. W. Dever, H. J. Fraser and M. R. S. McCoustra, *Astrophys. Space Sci.*, 2003, **285**, 633–659.
63 J. Hohlfeld, S.-S. Wellershoff, J. Güdde, U. Conrad, V. Jähnke and E. Matthias, *Chem. Phys.*, 2000, **251**, 237–258.
64 V. Damian and M. Oane, *Lasers Eng.*, 2016, **33**, 181–187.
65 S. L. Sobolev, *Int. J. Heat Mass Transfer*, 2016, **94**, 138–144.
66 J. He, K. Acharyya and G. Vidali, *Astrophys. J.*, 2016, **825**, 89.
67 F. Perakis, L. De Marco, A. Shalit, F. Tang, Z. R. Kann, T. D. Kühne, R. Torre, M. Bonn and Y. Nagata, *Chem. Rev.*, 2016, **116**, 7590–7607.
68 C.-C. Yu, K.-Y. Chiang, M. Okuno, T. Seki, T. Ohto, X. Yu, V. Korepanov, H. Hamaguchi, M. Bonn, J. Hunger and Y. Nagata, *Nat. Commun.*, 2020, **11**, 5977.
69 S. Woutersen and H. J. Bakker, *Nature*, 1999, **402**, 507–509.
70 H. Arnolds, C. Rehbein, G. Roberts, R. J. Levis and D. A. King, *J. Phys. Chem. B*, 2000, **104**, 3375–3382.
71 A. Srinivasa Rao, *Optik*, 2022, **267**, 169638.
72 W. L. Peticolas, *Annu. Rev. Phys. Chem.*, 1967, **18**, 233–260.
73 A. M. Bonch-Bruevich and V. A. Khodovoĭ, *Sov. Phys. Uspekhi*, 1965, **8**, 1–38.
74 J. D. McDonald, *Annu. Rev. Phys. Chem.*, 1979, **30**, 29–50.
75 V. E. Bondybey, *Annu. Rev. Phys. Chem.*, 1984, **35**, 591–612.
76 S.-I. Chu and D. A. Telnov, *Phys. Rep.*, 2004, **390**, 1–131.
77 P. Sudera, J. D. Cyran, M. Deiseroth, E. H. G. Backus and M. Bonn, *J. Am. Chem. Soc.*, 2020, **142**, 12005–12009.
78 S. Taj, D. Baird, A. Rosu-Finsen and M. R. S. McCoustra, *Phys. Chem. Chem. Phys.*, 2017, **19**, 7990–7995.
79 S. Taj, D. Baird, A. Rosu-Finsen and M. R. S. McCoustra, *Phys. Chem. Chem. Phys.*, 2019, **21**, 21663–21664.

